5-2012

Bubble Coalescence and Breakup Modeling for Computing Mass Transfer Coefficient

Ryan A. Mawson
Utah State University

BUBBLE COALESCENCE AND BREAKUP MODELING FOR COMPUTING MASS TRANSFER COEFFICIENT

by

Ryan A. Mawson

A thesis submitted in partial fulfillment
of the requirements for the degree

of

MASTER OF SCIENCE

in

Mechanical Engineering

Approved:

Dr. Robert E. Spall Major Professor	Dr. Thomas H. Fronk Committee Member
Dr. Barton Smith Committee Member	Mark R. McLellan Vice President for Research and Dean of the School of Graduate Studies

UTAH STATE UNIVERSITY
Logan, Utah

2012

ABSTRACT

Bubble Coalescence and Breakup Modeling

for Computing Mass Transfer Coefficient

by

Ryan A. Mawson, Master of Science

Utah State University, 2012

Major Professor: Dr. Robert E. Spall
Department: Mechanical and Aerospace Engineering

There exist several different numerical models for predicting bubble coalescence and breakup using computational fluid dynamics (CFD). Various combinations of these models will be employed to model a bioreactor process in a stirred reactor tank. A mass transfer coefficient, $K_l a$, has been calculated and compared to those found experimentally by Thermo-Fisher Scientific, to validate the accuracy of currently available mathematical models for population balance equations. These include various combinations of bubble breakup and coalescence models coupled with the calculation of mass transfer coefficients.

(58 pages)

PUBLIC ABSTRACT

Bubble Coalescence and Breakup Modeling for Computing Mass Transfer Coefficient

By Ryan Mawson, Master of Science
Utah State University, 2012

Modeling fluid behavior with computer numerical models can be very difficult due to the physical phenomenon which can be present in complex fluid systems. One difficult situation to model is when there is more than one type of fluid in a system. Some of these systems include fluids which do not mix, such as is the case when a liquid and a gas are present. In this situation, the gas phase will form bubbles which are dispersed throughout the liquid phase. Modeling the breakup and coalescence of these bubbles is critical to correctly model this type of situation.

There exist several different numerical methods for modeling bubble coalescence and breakup in computational fluid dynamics (CFD). Various combinations of these models have been employed to model a bioreactor process in a stirred reactor tank. A mass transfer coefficient, $K_l a$, has been calculated and compared to those found experimentally by Thermo-Fisher Scientific. The purpose is to validate the accuracy of currently available mathematical models for population balance equations (including various combinations of bubble breakup and coalescence models) coupled with the calculation of mass transfer coefficients.

DEDICATION

Special thanks are given to my wonderful wife, Jennie, for her great patience and support in this lengthy endeavor.

Thanks are also due to my major professor Dr. Spall, for starting this project, and to each of the listed committee members for their professional and academic assistance and comments.

CONTENTS

LIST OF TABLES

LIST OF FIGURES

CHAPTER I

INTRODUCTION

Modern computational fluid dynamics programs have become quite comprehensive. CFD is employed ever more increasingly as a tool to validate designs in order to save money and ensure success. One of the areas where there is a large demand for CFD is in modeling bioprocesses and chemical processes. Pharmaceutical and other related industries are growing at an ever-increasing pace, and placing greater importance on the ability to model the processes they employ for their products. Bioreactors are one method of production which is used for many of these processes. The ability to predict how bioreactors of increasing size and/or complexity will perform is critical to the success of these companies. In doing this, it is crucial to have methods for CFD which are proven and which can be relied upon with some degree of certainty. One of the areas requiring more validation is that of population balance models being used in modeling these situations. A population balance model involves models for bubble coalescence and breakup in order to model the bubbles of air or other fluid in a two-phase system. The present work will compare the use of different bubble coalescence and breakup models, and different numbers of bins of bubbles in a 250-L impeller-stirred bioreactor tank. Specifically, the volume averaged value of the mass transfer coefficient will be compared between these cases, and with available experimental results.

In many bioprocesses, oxygen is one of the limiting factors of the process. This limitation can impede the progress of a reaction, or make the reaction impossible to carry out on a production scale. One way to solve this problem is to use a bioreactor setting for carrying out a bioprocess. These bioprocesses can be more tightly controlled, and the

necessary oxygen can be fed into the system, allowing the reaction or process to be carried out much more efficiently or quickly.

CHAPTER II

LITERATURE REVIEW

Gigas and Dhanasekharan [1] used a multiphase Eulerian model to validate the mass transfer coefficient for a cell-culture reactor, which is an aerobic bioreactor. They employed the FLUENT software package to compute the mass transfer coefficient of the process and model the cell-culture reactor. They were able to get the CFD $K_l a$ number to agree satisfactorily with their $K_l a$ found experimentally. Once these numbers were sufficiently close, they used a population balance approach for the gas phase, and the Sauter mean diameter to calculate the interphase drag between the gas and the liquid. This Sauter mean diameter was calculated from the bubble size distribution. They found that after validating the model to this point, the results compared fairly closely with a commonly used correlation. They computed a volumetrically averaged $K_l a$ number for the bioreactor which depends on the bubble size distribution to get the interfacial area, a, and the eddy dissipation, Schmidt number, and bubble size distribution to compute K_1.They reported that from their findings, the $K_l a$ number they calculated was within an order of magnitude of the experimentally determined $K_l a$ with the same operating conditions.

Fang's review paper [2] explained in depth the types of CFD modeling processes, mesh options available, and the basic equations of CFD modeling in bioprocesses and other similar processes. He describes CFD use in the pharmaceutical industry (which is one of the largest industries employing CFD modeling) to ensure the success of bioreactors and processes as they are scaled-up from model to production. Current CFD methods are being continually improved so that pharmaceutical companies (and others)

can better benefit from their use. Bioprocesses are most efficient when they are controlled within their optimal operating conditions. These operating conditions are usually different for each individual process. These processes may not otherwise be able to proceed successfully. Using CFD methods to model processes can better ensure their success.

One of the most important points Fang makes is that these complex situations require an expert in CFD to ensure the physics are modeled correctly. There are many limitations on the correct use of CFD modeling. If these are not understood, the results obtained may be erroneous. One must be able to rely on the results obtained, especially if there are products or processes being developed based on these results. Choosing the correct models, methods, and applications for CFD is critical to ensure the accuracy of the solution. Fang points out that some areas of CFD which still require extensive research include the modeling of bubble breakup and coalescence. Fang also notes that with any CFD modeling, it is critical to compare the results to some well-proven model or experimental results in order to validate the solution(s) achieved.

Bayraktar et al. [3] cover some of the main points about bubble breakup and coalescence models. They point out that each has limitations and weaknesses. These methods are all different and can vary dramatically one from another. This seems to suggest that it would be difficult to get these models to agree with any degree of accuracy. These models generally rely on similar principles of physics to describe what is happening with the phases included. Most bubble coalescence models are based on the idea that bubbles close together will tend to merge together if there are no turbulent eddies present. These turbulent eddies tend to cause bubble breakup when they collide

with bubbles and area able to overcome the surface tension of the bubble. Bayraktar et al. [3] state that it would be easy to spend too much effort trying to model a process if there is not sufficient information and understanding regarding the physics of the problem in order to model it correctly. It is important to consider all implications of using different available numerical models in any CFD modeling case. Bayraktar et al. [3] introduce the idea of a population balance equation. This is a numerical method for describing how bubbles are distributed, according to size, in a two-phase system or flow. There are several different population balance formulations, differing somewhat one from another. These population balance equations make it possible to model larger amounts of bubbles or bubbles which are widely dispersed with less computational resources and time. In methods of CFD, it is important to balance time and resources with results desired.

Turbulence models are also important in capturing the true physics of CFD problems. These models are critical in high-Reynolds number flows, or otherwise turbulent regimes. Without these turbulence models, the physics of the actual problem will not be properly conveyed. Bayraktar et al. [3] describe one of the most well-known turbulence models used in CFD; the k-epsilon model. This is the model they chose to use in their research. Because of the accuracy of this model in modeling turbulent flows, it is one of the most widely used available. Bayraktar et al. [3] go on to describe with quite a bit of detail, the coupling of population balance equations with turbulence models in multi-phase flows. The reader is referred to their work for a further explanation of how this coupling is achieved and how it is implemented in CFD modeling. This will not be further discussed in the present work.

Lehr et al. [4] have developed a new method for modeling bubble size distribution in bubble column type reactors. These types of bubble columns are used in many different bioprocesses and other chemical processes. They developed and implemented a formulation which predicts the bubble volumes in these bubble columns.

In bioprocesses and chemical processes, the distribution of bubbles of different sizes is constantly changing. This is not a steady-state type of process, so this is to be expected. Since these flow fields are highly complex, it is difficult to model this type of bubble phenomena without extensive computational resources. These numerical simulations can be realized by the Euler-Euler method or the Euler-LaGrange method. The Euler-LaGrange method models each of the bubbles individually, or as separate entities. The Euler-Euler method simulates the bubbles as a semi-continuous phase, which requires far less computational resources. Each of these methods has advantages to their use. The Euler-LaGrange method is a more accurate model of the actual physical characteristics of the problem, but requires greater resources. The Euler-Euler method requires far less resources and is sufficient for most cases where the average behavior of the system is sufficient for the problem being solved.

Lehr et al. [4] go on to describe in detail the formulation of bubble breakup and coalescence models. These models are quite complex and the reader is referred to their work for a deeper understanding of these models, if such understanding is desired. One important point is that the authors point out that bubbles which come into contact with a turbulent eddy in the flow field, generally break up into a smaller and a larger bubble, rather than many small bubbles or equally-sized bubbles. This does depend on the strength of the eddy, and affects the calculation of the mass transfer coefficient. The work

done by Lehr et al. [4] does not cover the calculation of mass transfer coefficients. Their work is also limited to columns up to 0.3 meters (~1 foot) in diameter.

Lehr and Mewes [5] use a population balance equation to model the bubble size distribution in bubble columns. They introduce new kernel functions for the breakup and coalescence of these bubbles, which allows them to simplify the population balance equation to a transport equation. This is easier to solve and requires less computational resources. The distribution of bubbles of different sizes in a multi-phase system is critical to the calculation of transfer coefficients for mass and energy. Thus, having a model which accurately predicts bubble size distribution is critical to calculating these transfer coefficients accurately.

Lehr and Mewes [5] note that the actual bubble size distribution in a process is difficult to predict accurately since there are severe limitations on the number of phases which can be used in a model. This limitation is due to the limitations of current CFD modeling techniques and the need for extreme amounts of computer resources.

Lehr and Mewes [5] developed a transport equation for the average bubble volume in the system, which is implemented into a commercial CFD code. This simplified average bubble volume equation gives the possibility of using less computational resources while still achieving sufficiently accurate results, since only one other transport equation needs to be solved. Having fewer equations to solve usually means less computational resources are required to solve the problem. Lehr and Mewes [5] applied their simplified equation to a commercial CFD code with a two-phase Euler-Euler model. A standard k-ε model is employed for simplicity, but they do consider the source terms and dissipation rate. They use local values of bubble volume to calculate the interface transfer terms between the

two phases. They perform calculations for transient flow in three dimensions. Again, they find that for their process, the distribution of bubbles is not homogenous, not stationary, and changes with time. Through their work, they are able to model the formation of large bubbles as part of the bubble size distribution. Others have not been able to formulate large bubbles. Their work is also limited to bubble columns of less than about 0.3 meters (~1 foot) in diameter.

Milles and Mewes [6] state that the prediction of interfacial area density is one of the critical parameters in predicting mass, energy, and momentum transfer in bioprocesses and chemical processes. The design of reactors depends greatly on these calculations. Milles and Mewes [6] focus their research on the steady state which bubble breakup and coalescence can reach, after the system being modeled has sufficient time to run. The bubbles must have a sufficient residence time in the system in order to reach this steady state. The residence time of the bubbles is the amount of time the bubbles are in the secondary fluid, during the process. They use a single population balance equation to model the breakup and coalescence of bubbles in their process. Milles and Mewes' [6] research is mostly focused on the effects of additives on the bubble population balance equation.

Kerdouss et al. [7] took an approach very similar to that proposed herein, but did not apply different population balance equations to the problem. They introduce the idea of Sliding Mesh (SM) and Multiple Reference Frame methods for adding an impeller to a bioreactor. These methods reduce the computational power needed for these types of simulations. They use a relatively small bioreactor setup for their work (2 L working capacity). This limits the cases in which their results are proven, and may limit the cases

where those results could be applicable. In the numerical model, they apply well-known mathematical equations for turbulence, governing flow, and others as needed. They employed the FLUENT program for their work. They employ a single population balance model with a single bubble breakup model and a single bubble coalescence model. As in other previous works, they have employed a multiple reference frame approach for modeling the region directly about the impeller. This decreases the computational time and resources needed for the simulation, as has been previously mentioned. Their population balance models included different numbers of bins in different cases. They also applied a model with a single common bubble size. It was observed that the $K_l a$ computed by the population balance model was the closest value to that found experimentally. They only used 7, 9, 11, and 13 bubble classes for their population balance model. They found that with higher numbers of classes, the results seemed more accurate. In computing the mass transfer coefficient, they applied equations to calculate the average bubble diameter (and thus calculate the average interfacial bubble area) and to calculate the average K_l. Once the averages were calculated, they were multiplied to get the local and overall average $K_l a$.

Spall et al. [8] applied computational fluid dynamics to modeling single-use bioreactors. Cases were run for bioreactors of different sizes and with different impeller rpm. An Eulerian-Eulerian model for the two-phase flow was employed to model the fluids in the system. An approach using a multiple reference frame was employed in order to speed up calculations and minimize computational resources required. Models were created in 50-L, 250-L, and 2,000-L cases with similar setups. Spall et al. [8]

compare dimensionless power numbers, general flow patterns, and mass transfer coefficients from these results.

In the general model setup, an Eulerian model was employed for each phase in the model, having mass and momentum equations solved for each phase. The FLUENT 12.0.3 software was used for this work. A tetrahedral mesh was created using the preprocessor GAMBIT, and then imported to the FLUENT software. This mesh was converted to a polyhedral mesh for improved convergence characteristics. For the 250-L bioreactor, the mesh consisted of just over 2.2 million cells, thus requiring a multi-processor cluster computer system to make calculations possible and efficient. Simulation was carried out with the multiple reference frames around the impeller region. Once the multiple reference frame approach had reached a steady state, the sliding mesh model (SMM) was also separately applied, using the MRF results as a starting condition.

Spall et al. [8] found that the maximum velocities inside the tank were approximately 1.2-1.5 m/s. They found that differences between the SMM and MRF models were small when comparing velocity. Their results for velocity fields compare well between the SMM and MRF models and what would be expected. Mixing times were estimated and found to be approximately 10 seconds for the 50-L tank, and up to 30 seconds for the 2000-L tank. These mixing times depend on impeller rotation rate. The power required to rotate the impeller at the desired rate was also calculated for these cases. They found that the calculated power numbers showed the general trend of more power required with larger tank volume. They also performed grid convergence studies to ensure accuracy of their achieved results. They found that the results were sufficiently grid converged for the models employed.

The mass transfer calculations were performed using equations presented by Kerdouss et al. [7] and Dhanasekharan et al. [9]. Their method of calculating the product of Kl and a, then volume averaging the result was employed. Spall et al. [8] present results for the 250-L tank volume with an impeller rotation rate of 118 RPM only. The reader is referred to the results presented by Spall et al. [8] it is sufficient for the present work to state that the computed values of $K_l a$ depend highly on the Sauter mean bubble diameter (since the interfacial bubble area depends heavily on the diameter of the bubbles found in the system). The computed $K_l a$ also depended heavily on the bubble diameter in the constant bubble diameter cases (the larger the bubble diameter, the smaller the $K_l a$). They also found that bubble coalescence was much more likely to occur than bubble breakup. This coalescence appeared to largely dominate the system.

CHAPTER III

OBJECTIVES

This work extends the previous analysis of Spall et al. [8]. In particular, the following objectives will be accomplished.

- Set up cases for different population balance equation combinations.
    - Include 12 combinations of the following bubble breakup and coalescence models:
        - Breakup models: Luo model, Lehr model, Ghadiri model, and Laakkonen model.
        - Coalescence models: Free-molecular model, Luo model, and Turbulent model.
    - Include cases with different numbers of bubble "bins."
        - Cases will be setup with 7, 11, 13, and 15 bins (Results for 9 bins available in Ref. [8]).
    - Run several cases with constant bubble diameters.
        - Cases will be run with 0.5, 1, 1.5, and 2 mm diameter bubbles.
- Run all cases with the FLUENT software package on the USU Cluster.
    - Reference points are the results presented in Ref. [8].
    - Cases will be iterated upon until the computed $K_l a$ numbers have converged.
- Analysis of results
    - Compare calculated $K_l a$ numbers to each other and to experimental results from Thermo Fisher Scientific.

  - Compare velocity profiles throughout computational volume.
  - Compare particle tracks and velocity vectors between cases and to original case to ensure similarity.

- Determine from results whether or not current methods for modeling bubble breakup and coalescence are sufficient for computing accurate mass transfer coefficients.

CHAPTER IV

APPROACH FOR MEETING OBJECTIVES

Each configuration to be investigated is setup in the FLUENT CFD software in terms of parameters such as bubble coalescence and breakup models.

Once these cases configured, each will be run on the USU High-Performance Computing cluster. In an initial work [8], it was found that up to 20,000 iterations were needed to reach convergence in general cases. It is expected that the number of iterations will be significantly less since subsequent cases will be started from previously converged cases. However, there may be different numbers of iterations required for each different case in order to reach convergence (residuals at 10^{-3} or lower).

Once each case has reached convergence, the results will be analyzed and compared. These results will be presented in the form of velocity profiles, contours of bubble densities, or other relevant graphics. The $K_l a$ number from each case will be presented and the results discussed.

CHAPTER V

HYPOTHESIS

One possible outcome is that there will be combinations of bubble coalescence and breakup models which will be sufficient for allowing the calculation of a $K_l a$ number which is close to that found experimentally. The second possibility is that the current numerical models which exist for modeling bubble coalescence and breakup are not sufficient to accurately calculate a $K_l a$ number.

At this time, I feel it is difficult to accurately predict such a coefficient as a $K_l a$ number due to the complexity of bubble coalescence and breakup. From the results of past work done by others, it is clear that the $K_l a$ number depends heavily on several factors including the Sauter mean bubble diameter or the diameter of the bubbles in a system if using a constant bubble diameter input. It would be easily conceivable to find mass transfer coefficients which vary greatly even with a small change in bubble diameter over the calculation volume.

CHAPTER VI

SETUP OF CASES

The initial case presented in Spall et al. [8] used the Luo bubble coalescence model, and the Lehr bubble breakup model, both of which are included in the FLUENT Version 13.0 software package. There were 9 bubble size bins used for the initial case. The largest bubble diameter was set to 0.00806349 m, while the smallest bubble diameter was 0.0002 m. The ratio exponent q was set to 2. The K_v value was set to the default value of $\pi/6$, where K_v is the particle volume coefficient, used to calculate the volume of the bubbles of oxygen in this model. The growth rate based on particle diameter is given by:

$$G = \frac{\partial L}{\partial t} \tag{1}$$

where $\partial L/\partial t$ is the time rate of change of the bubble diameter, and G is the growth rate based on particle diameter.

The volume of a single particle V is given by:

$$V = K_v L^3 \tag{2}$$

where L is the length (or diameter) of the respective bubble ($L = d$ *for spheres*). Then, the growth rate based on particle volume, G_v, is given by the following equation.

$$G_v = 3K_v L^2 G \tag{3}$$

The surface area of a particle is given by Eq. 4. Where again, L is the bubble diameter for this situation, assuming spherical oxygen bubbles.

$$A = 6K_v L^2 \tag{4}$$

The Bubble bins and their associated sizes are listed in Table 1. The 9-bin case by Spall et al. [8] was run for approximately 20,000 iterations in order to decrease residuals

to order 10^{-4} [8]. The other bin numbers were run in separate cases for the current work. In running such a large number of iterations of such a complicated CFD case, a simple desktop computer would not have been sufficient. With much more extensive computer resources, these cases were run much more quickly. Multiple cases were run concurrently in order to achieve the desired results with the different model combinations.

Table 1: Numbers of bubble bins with corresponding minimum and maximum diameters.

Number of Bins	Maximum Bubble Diameter (m)	Minimum Bubble Diameter (m)
7	0.008063	0.000200
9	0.003200	0.000200
11	0.020319	0.000200
13	0.051200	0.000200
15	0.129016	0.000200

Figure 1 gives a depiction of the geometry of the tank, including the impeller, the impeller shaft, and the sparger at the bottom of the tank.

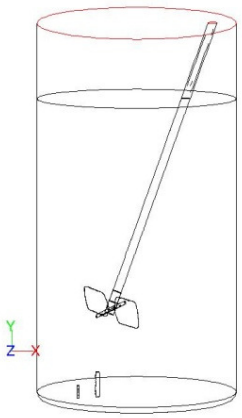

Fig. 1: View of geometry of tank setup.

The mesh employed was a high quality mesh to ensure the accuracy of the calculations. The mesh consisted of 437,044 polyhedral cells. The orthogonal quality of

the cells is shown in a histogram in Figure 2. The number of cells near zero (worse quality) is very insignificant. The majority of the cells are skewed to close to 1, indicating a good quality mesh.

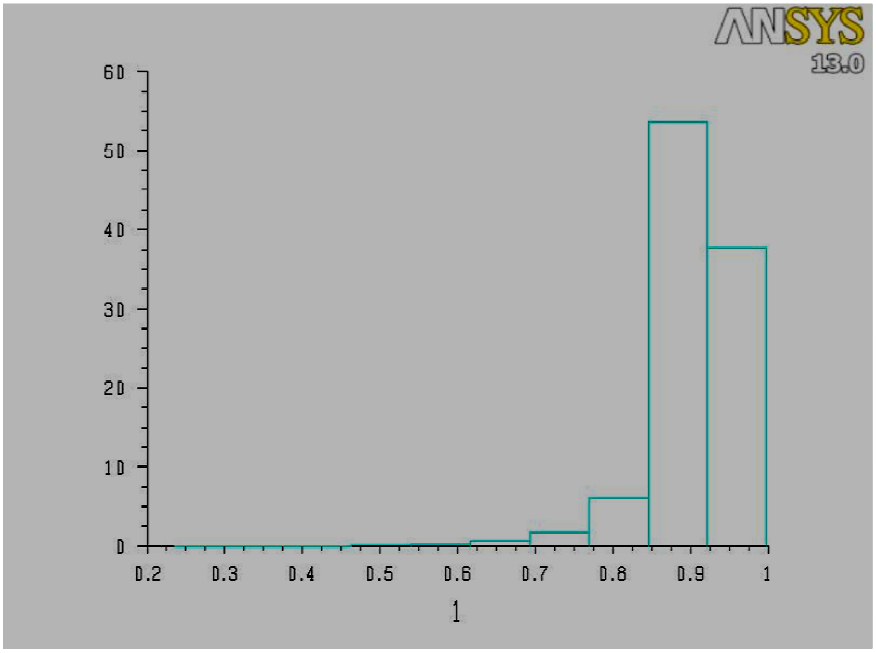

Fig. 2: Histogram showing orthogonal quality of the cells in the mesh.

The mesh is a very important part of the solution to a numerical problem such as this. A poor quality mesh can lead to incorrect or inaccurate solutions, or solutions with less-than-sufficient resolution to capture the true behavior of the fluid(s) being modeled. Figures 3-5 give different views of the mesh, as used in the initial case done by Spall et al. [8]. Recall that a sliding mesh model was used to model the impeller region. This SMM mesh can be clearly seen in Fig. 3. The mesh including the air and the separate volumes of air and liquid can be seen in Figs. 3 and 4.

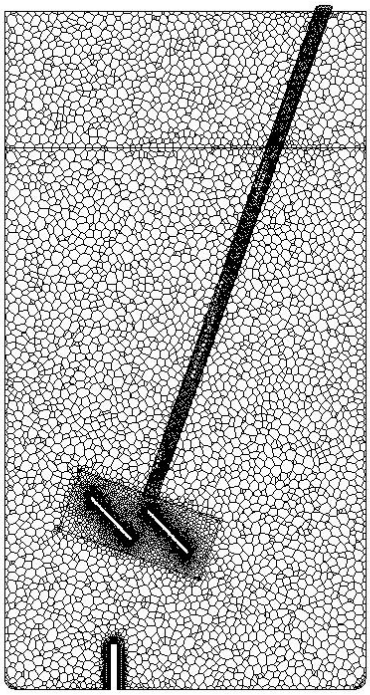

Fig. 3: View of full tank mesh, showing polyhedral cells.

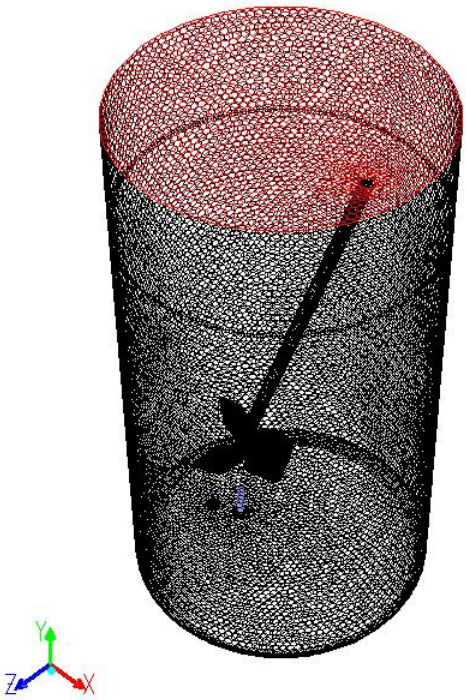

Fig. 4: Isometric view of full tank mesh.

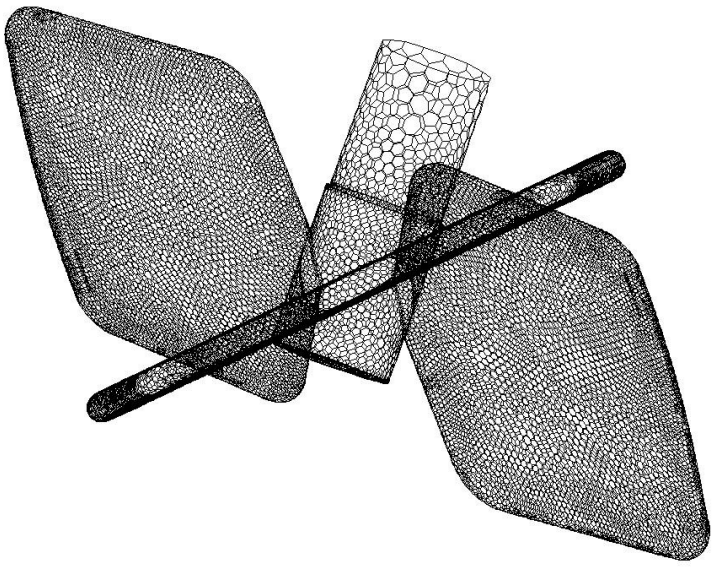

Fig. 5: View showing mesh on impeller surface.

There are several different combinations of bubble coalescence and breakup models available for use in the FLUENT 13.0 software. The three coalescence models which will be used include the Luo model, the Lehr model, and the Free-Molecular model [10]. The bubble breakup kernel formulations include the Luo model, the Lehr model, the Ghadiri model, and the Laakkonen model [10]. These do not represent all possible bubble breakup and coalescence models available, but give a good representative sample for the purposes of this work. In reality, there are a large number of conceivable combinations of these models with multiple different parameters, which the user could adjust. The FLUENT software package also includes the ability for the user to apply any other version of equation, as these can be input into the software by the user.

In each of the combinations, the default values for coefficients and parameters were chosen for simplicity. Again, there are a large number of possible combinations of the

population balance equation which can be run since these parameters are easily adjusted to nearly any desired value.

For the bubble aggregation (coalescence) kernel functions, the following default parameters were used in the simulations. For the Turbulent model, the Hamaker Constant was set to 2.3e-20. For the Luo aggregation kernel, the surface tension coefficient was set to 0.07 N/m, which is the default for water. For the Luo breakage kernel function, the surface tension was also chosen as 0.07 N/m. For the Lehr breakage kernel function, the surface tension used was 0.07 N/m and the critical Weber number was set to 0.1. For the Ghadiri breakage kernel function, the breakage constant was set to 8e+08, the default value. For the Laakkonen breakage kernel function, the surface tension was again set to 0.07 N/m. These values were chosen due to simplicity only, there was no effort made to match these numbers to any given reference points or other data sets or results. These parameters were all the default values stored in the FLUENT 13.0 program. All cases were run in double precision mode in the FLUENT software.

Initially, 20 cases were setup to run with the different models available. These cases are presented in Table 2. The cases consisted of the different combinations of the aforementioned bubble aggregation and breakup models. For the cases which had the same bubble aggregation models, there were no other parameters changed, other than the breakup kernel functions. This allows the comparison of cases of the same aggregation models while having no other influences from any other changes to the cases. The cases run with constant bubble diameters were also done in similar manner. Since there are no bubble breakage or aggregation kernels in this case, the diameter was the only thing varied between the cases. The cases where different numbers of bins were applied used

the same combination of the Luo bubble breakage model and Lehr aggregation kernel function.

Table 2: Configuration of initial 20 cases.

Aggregation Model	Breakup Model	Cases	Difference
Luo Model [10]	Lehr Model	A1	Original case run by Spall et al.
Luo Model	Lehr Model	B1 - bubble bins	Cases run with different number of bubble bins (See Table 1 for sizes)
Luo Model	Lehr Model	B2 - 11 bubble bins	
1. Luo Model	Lehr Model	B3 - 13 bubble bins	
2. Luo Model	Lehr Model	B4 - 15 bubble bins	
Luo Model	Lehr Model	C1 – 0.5 mm dia. Bubbles	Constant Bubble Diameter Cases
Luo Model	Lehr Model	C2 – 1.0 mm dia. bubbles	
Luo Model	Lehr Model	C3 – 1.5 mm dia. bubbles	
Luo Model	Lehr Model	C4 – 2.0 mm dia. bubbles	
Luo Model	Luo Model	D1	Cases Run With Different Bubble Aggregation and Breakup Model Combinations. Cases D1 - F4 were run with 9 bubble bins (same as Case A1).
Luo Model	Ghadiri Model	D2	
Luo Model	Laakkonen Model	D3	
Free-Molecular Model [10]	Luo Model	E1	
Free-Molecular Model	Lehr Model	E2	
3. Free-Molecular Model	Ghadiri Model	E3	
Free-Molecular Model	Laakkonen Model	E4	
Turbulent Model [10]	Luo Model	F1	
Turbulent Model	Lehr Model	F2	
Turbulent Model	Ghadiri Model	F3	
Turbulent Model	Laakkonen Model	F4	

As mentioned previously, each of the cases was run with the same Realizable k-ε turbulence model with enhanced wall treatment and a dispersed multiphase turbulence model approach. The remaining general model constants and numbers used are as follows: the TKE Prandtl Number was set to 1, the TDR Prandtl Number was set to 1.2, and the Dispersion Prandtl Number was set to 0.75. All other constants and variables

were chosen to be the default values from the FLUENT software package unless otherwise specified. This was done for simplicity only.

CHAPTER VII

BUBBLE AGGREGATION KERNEL FUNCTIONS

The bubble aggregation kernel functions used were the Free-molecular model, the Luo model, and the Turbulent model. Each of these is different in the formulation of the equations which attempt to numerically model the aggregation of bubbles in a system. The equations for these models have been developed and derived by others and will not be presented here. Only the basics of the models used will be described below. The reader is referred to the literature for a more in-depth discussion of the derivations of each of the population balance kernel functions and their characteristics.

The free-molecular model uses the idea that the frequency of collision, and therefore aggregation, is size dependent and Eq. 5 is applied as follows:

$$a(L_i, L_j) = \frac{2k_B T}{3\mu} \frac{(L_i + L_j)^2}{L_i L_j} \tag{5}$$

where α is the frequency of bubble collisions of bubbles i and j, k_B is the Boltzman constant, T is the absolute temperature, μ is the dynamic viscosity of the fluid, L_i and L_j are the diameters of bubbles i and j, respectively (adapted from ANSYS 2010 [10]).

The Luo model uses a general kernel equation defined as the rate of particle volume formation as a result of binary collisions of particles with volumes V_i and V_j, given by Eq. 6 as:

$$\Omega_{ag}(V_i, V_j) = \omega_{ag}(V_i, V_j)\, P_{ag}(V_i, V_j)\ [m^3/sec] \tag{6}$$

where ω_{ag} is the frequency of collision and is given by Eq. 7:

$$\omega_{ag}(V_i, V_j) = \frac{\pi}{4} \left(d_i^2 + d_j^2\right) n_i n_j \bar{u}_{ij} \tag{7}$$

Here $\bar{u}_{ij}$ is the characteristic velocity of collisions of two particles with diameters d_i and d_j and number densities n_i and n_j. The mixing velocity $\bar{u}_{ij}^t$ of these two particles is given by Eq. 8:

$$\bar{u}_{ij}^t = \left(\bar{u}_i^2 + \bar{u}_j^2 \right)^{1/2} \tag{8}$$

and $\bar{u}_t$ is given by Eq. 9:

$$\bar{u}_i = 1.43 \, (\varepsilon d_i)^{1/3} \tag{9}$$

P_{ag} is the probability of a collision resulting in coalescence of bubbles. The probability is given by Eq. 10:

$$P_{ag} = \exp\left(-c_1 \frac{\left[0.75\left(1+x_{ij}^2\right)\left(1+x_{ij}^3\right)\right]^{\frac{1}{2}}}{\left(\frac{\rho_2}{\rho_1}+0.5\right)^{\frac{1}{2}}\left(1+x_{ij}\right)^3} We_{ij}^{\frac{1}{2}} \right) \tag{10}$$

Here c_1 is a constant of order unity, $x_{ij} = d_1/d_2$, ρ_1 and ρ_2 are the densities of the primary and secondary phases, respectively. We_{ij} is the Weber number, given by Eq. 11.

$$We_{ij} = \frac{\rho_1 d_i \left(\bar{u}_{ij}^t\right)^2}{\sigma} \tag{11}$$

The turbulent aggregation kernel assumes that aggregation occurs by either a viscous subrange mechanism or by an inertial subrange mechanism. The viscous subrange mechanism is applied when particles are smaller than the Kolmogorov microscale, η. The inertial subrange mechanism is applied when particles exceed the Kolmogorov microscale. In the case of the inertial subrange mechanism, particles assume individual velocities (different for each particle). The Kolmogorov scale is given by Eq. 12:

$$\eta = \left(\frac{\nu^3}{\epsilon}\right)^{1/4} \tag{12}$$

where ν is the kinematic viscosity of the fluid and ϵ is the turbulent energy dissipation rate.

The collision rate for the viscous subrange is given by Eq. 13:

$$a(L_i, L_j) = \zeta_T \sqrt{\frac{8\pi}{15}} \dot{\gamma} \frac{(L_i + L_j)^3}{8} \tag{13}$$

where ζ_T is a pre-factor taking into account the capture efficiency coefficient of turbulent collision and $\dot{\gamma}$ is the shear rate. It is given by Eq. 14:

$$\dot{\gamma} = \frac{\epsilon^{1/2}}{\upsilon} \tag{14}$$

For the inertial subrange, the particles are larger than the smallest eddy present in the system, so they are dragged by velocity fluctuations in the flow field. The aggregation rate is expressed in Eq. 15:

$$a(L_i, L_j) = \frac{\zeta_T 2^{\frac{2}{3}} \sqrt{\pi} (L_i + L_j)^2}{4} \sqrt{(U_i^2 + U_j^2)} \tag{15}$$

where the last term is the root squared sum of the velocities for particles *i* and *j*.

The following equation (Eq. 16) describes the capture efficiency coefficient of turbulent collisions:

$$\zeta_T = 0.732 \left(\frac{5}{N_T}\right)^{0.242} \tag{16}$$

where N_T represents the ratio between the viscous force and the Van der Waals force, and should be NT ≥ 5. It is given by Eq. 17:

$$N_T = \frac{6\pi\mu (L_i + L_j)^3 \dot{\lambda}}{8H} \tag{17}$$

where $\dot{\lambda}$ is the deformation rate and *H* is the Hamaker constant. The deformation rate is given by Eq. 18:

$$\dot{\lambda} = \left(\frac{4\epsilon}{15\pi\nu}\right)^{1/2} \tag{18}$$

(adapted from ANSYS 2010 [10]).

CHAPTER VIII

BUBBLE BREAKUP KERNEL FUNCTIONS

The bubble breakup kernel functions used consisted of the Luo Model, the Lehr Model, the Ghadiri Model, and the Laakkonen Model. These models are all different in the formulations they use in order to calculate the bubble breakup in the simulation. They are all based on the idea that when bubbles run into eddies and the eddies are strong enough to break the bubble tension, then the bubbles will break apart. It has been observed that most often these bubbles will break into a larger one and a smaller one, not into two or more equally sized bubbles.

The Luo and Lehr Breakage kernels include both the breakage frequency and the PDF of breaking particles in the formulations. The breakage rate per unit volume is written as in Eq. 19:

$$\Omega_{br}(V,V') = \Omega_B(V')\eta\left(\frac{V}{V'}\right)[1/m^3/sec] \tag{19}$$

where the original particle has a volume *V'* and the daughter particle has a volume *V*. $\Omega_B(V')$ is the breakage frequency and $\eta(V/V')$ is the normalized daughter particle distribution function. In general, the equation is written as the integral over the size of eddies, lambda hitting the particle with diameter *d*. The volume would then be $V = \frac{4}{3}\pi\left(\frac{d}{2}\right)^3$ for a sphere. The integral is performed with bounds specified by the dimensionless eddy size $\xi = \frac{\lambda}{d}$ as follows, in Eq. 20.

$$\Omega_{br}(V,V') = K\int_{\xi_{min}}^{1}\frac{(1+\xi)^2}{\xi^n}\exp(-b\xi^m)\,d\xi \tag{20}$$

The Luo and Lehr models differ in the parameters (*K*, *n*, *b*, and *m*) which are input into the general equation above (adapted from ANSYS 2010 [10]).

For the Luo model, the following parameters (Eqs. 21-24) are used in the general equation:

$$K = 0.9238\varepsilon^{1/3} d^{-2/3}\alpha \quad (21)$$

$$n = 11/3 \quad (22)$$

$$b = 12\,(f^{2/3} + (1-f)^{2/3} - 1)\,\sigma\,\rho^{-1}\,\varepsilon^{-2/3}\,d^{-5/3} \quad (23)$$

$$m = -11/3 \quad (24)$$

For the Lehr model, the following parameters (Eqs. 25-28) are used in the general equation. These differ slightly from those above.

$$K = 1.19\,\varepsilon^{-1/3}\,d^{-7/3}\,\sigma\,\rho^{-1} f^{-1/3} \quad (25)$$

$$n = 13/3 \quad (26)$$

$$b = 2\,\sigma\,\rho^{-1}\,\varepsilon^{-2/3}\,d^{-5/3}\,f^{-1/3} \quad (27)$$

$$m = -2/3 \quad (28)$$

The Ghadiri model is used to model only the breakage frequency of the solid particles: in this case, the bubbles. The user should specify the PDF model for the daughter distribution of bubble sizes. In this model, the breakage frequency *f* is related to the material properties and impact conditions, as given in Eq. 29:

$$f = \frac{\rho_s E^{2/3}}{\Gamma^{5/3}}\, v^2 L^{5/3} = K_b v^2 L^{5/3} \quad (29)$$

where ρ_s is the particle density, *E* is the elastic modulus of the granule, *Γ* is the interface energy, *v* is the impact velocity, *and L* is the particle diameter prior to breaking. K_b is the breakage constant as defined by Eq. 30:

$$K_b = \frac{\rho_s E^{\frac{2}{3}}}{\Gamma^{\frac{5}{3}}} \quad (30)$$

(adapted from ANSYS 2010 [10]).

The Laakkonen model is given as the product of a breakage frequency *g(V')* and a daughter PDF *β(V,V')*. These are given by Eqs. 31 and 32:

$$g(V') = C_2 \varepsilon^{1/3} \, erfc\left(\sqrt{C_3 \frac{\sigma}{\rho_L \varepsilon^{\frac{2}{3}} d^{\frac{5}{3}}} + C_4 \frac{\mu_L}{\sqrt{\rho_L \rho_G} \varepsilon^{\frac{2}{3}} d^{\frac{5}{3}}}}\right) \tag{31}$$

and

$$\beta(V, V') = \frac{30}{V'} \left(\frac{V}{V'}\right)^2 \left(1 - \frac{V}{V'}\right)^2 \tag{32}$$

where $C_2 = 2.52$ is a constant, ε is the liquid phase eddy dissipation, $C_3 = 0.04$ is a constant, σ is the surface tension of the liquid phase, ρ_L is the liquid density, d is the parent particle diameter, $C_4 = 0.01$ is a constant, μ_L is the liquid dynamic viscosity, V' is the parent particle volume, and V is the daughter particle volume. The Laakkonen model is simple to compute, because of the simple daughter distribution equation (adapted from ANSYS 2010 [10]).

CHAPTER IX

RESULTS

The results from the described cases are presented here. They are limited to the cases described above, and for the conditions prescribed. These results are for the 250-L tank size, with an impeller which turns at 118 RPM. When the impeller turns at 118 RPM, the Reynolds number is 77,219. The impeller causes mixing of the fluid and eddies to form. The Reynolds number is calculated as follows:

$$Re = \frac{\rho D^2 N}{\mu} \tag{33}$$

where ρ is the density of the liquid, N is the rotation rate of the impeller (in rotations/sec), D is the diameter of the impeller, and μ is the dynamic viscosity of the liquid Spall et al. [8].

The results presented are for the MRF model mesh. Results include combinations of bubble coalescence and breakup models available in the FLUENT software, results for fixed bubble diameters of 1, 1.5, 2, and 2.5 *mm* each, and for bubble distributions of 7, 9, 11, 13, and 15 bins. The flow rate of the oxygen through the frit and into the tank was set at 2.5 *lpm* and the inlet bubble diameter was set to 2.12 *mm*, for all cases. The bubble diameter represents an estimate of the mean bubble diameter provided by Thermo Fisher Scientific.

The general flow pattern of the different cases all seem to agree well with that presented in Spall et al. [8]. Several velocity magnitude contour plots are presented here to show general flow patterns. This indicates that all the cases agree, at least qualitatively. Several of these representative velocity contour plots are shown in Figures 6-8. The velocity scales are not all equal, to give the reader a better visual picture of what is

happening in each of the cases. The air inlet tube can be seen at the bottom of the figures as a vertical white column. The impeller can also be seen near the bottom center of the tank. The water level can be seen as the rough line with some disturbance, near the top of the tank. The outline of the impeller volume can be seen clearly in Figure 7. In each of the figures, the velocity is the highest just around the impeller, as would be expected for mixing. There would also be the highest level of turbulence and bubble breakup in the region of the impeller. The velocity magnitude decreases with increasing distance from the impeller.

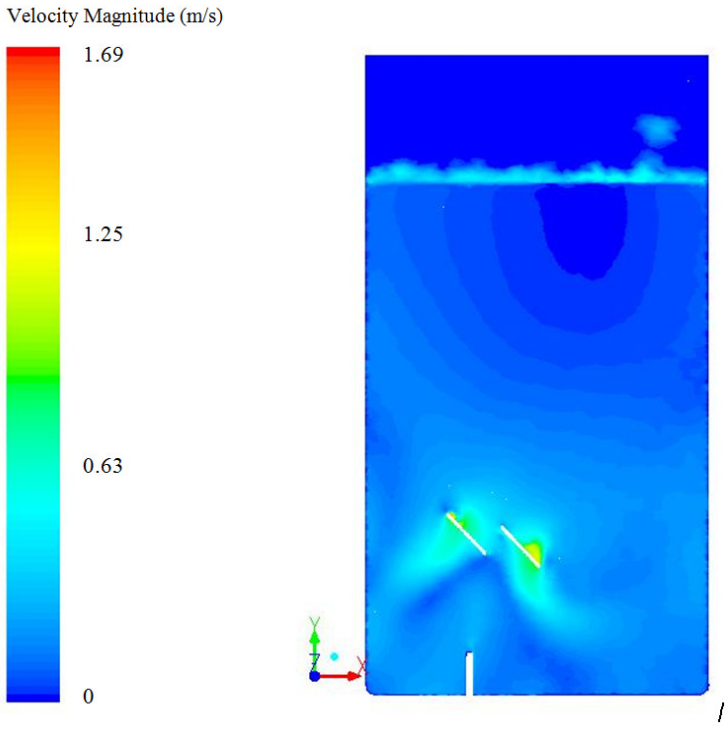

Fig. 6: Velocity magnitude contours for Case B2.

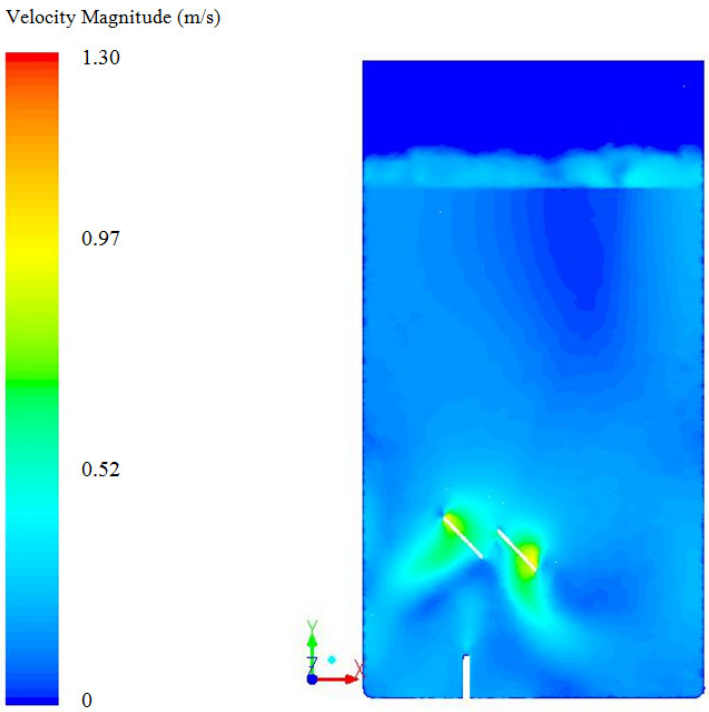

Fig. 7: Velocity magnitude contours for Case E1.

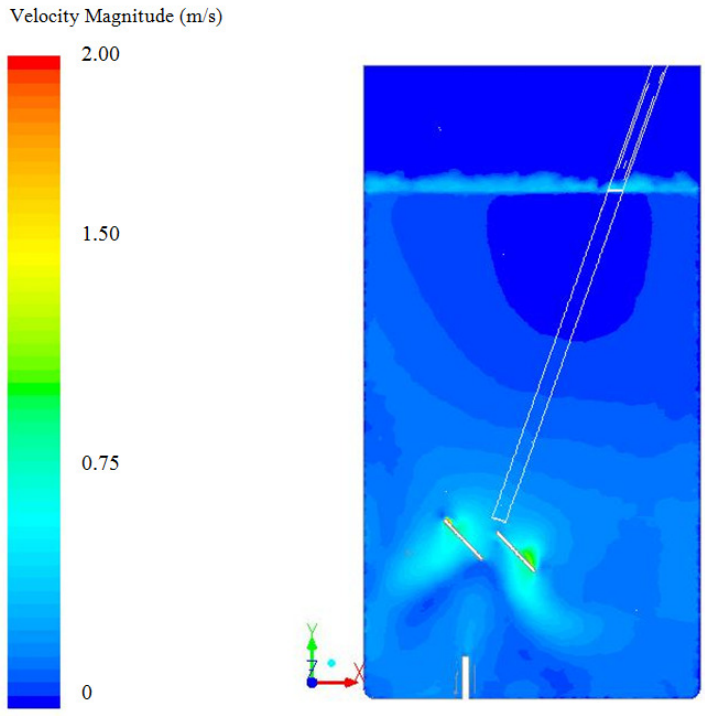

Fig. 8: Velocity magnitude contours for original Case A1.

Figures 9-13 show plots of velocity vectors for several representative cases. In these figures, the arrow lengths denote the magnitudes of velocities of the liquids in the region where the arrow tail is located. A longer arrow denotes a higher velocity magnitude and a shorter arrow denotes a lower velocity magnitude. It is clear from the figures that the cases have the same general flow patterns. In the lower right corner, there is an area of recirculation where the fluid creates a circular pattern in the X-Y plane, as shown by the velocity vectors. There also seems to be higher velocity fluid flowing faster past the impeller as it turns in the mixture, depicted by the concentration of arrows and the larger length of the arrows directly around the impeller. Figures 9-11 show the velocity vectors in the front plane, or the X-Y plane. Figure 12 shows the velocity vectors in the side plane, or the Y-Z plane. Figure 13 shows the velocity vectors in the X-Y plane, but a close-up view near the impeller, for better resolution in that region.

Due to the motion of the impeller, a high pressure region is created just below the impeller. Above the impeller, a low pressure region is created. This pressure difference causes the flow patterns to form a torroidal vortex about the impeller. More specifically, the fluid from the high pressure region below the impeller is drawn through the impeller and through the low pressure region above the impeller. This is similar to the phenomenon that causes the formation of a wingtip vortex during aircraft flight. This is most clearly seen in Fig. 13. A strong vortex can be seen at the lower right region of the figure.

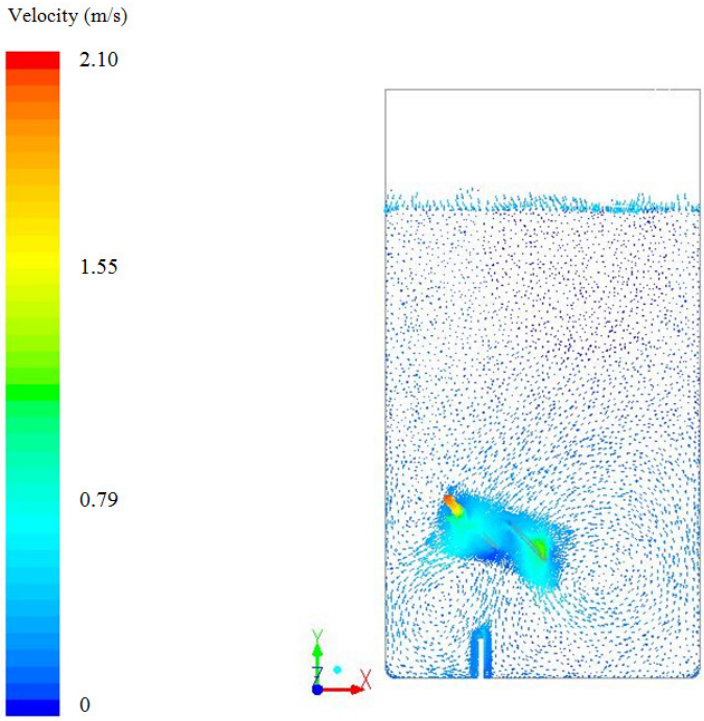

Fig. 9: Velocity vectors for Case B2.

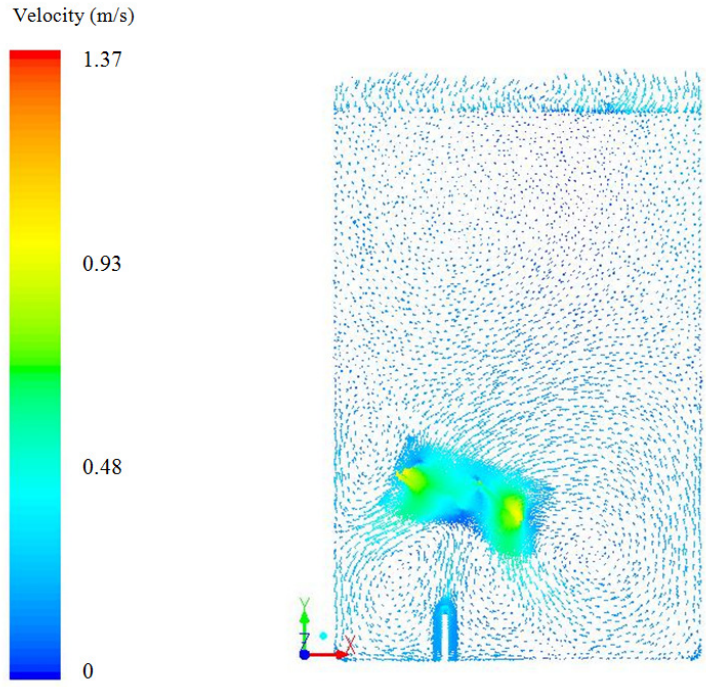

Fig. 10: Velocity vectors for Case E1.

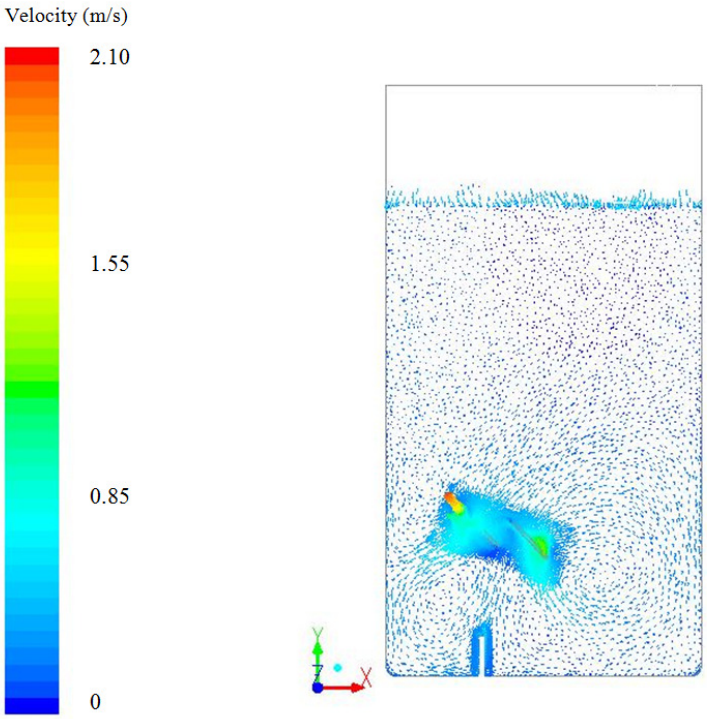

Fig. 11: Velocity vectors for original Case A1.

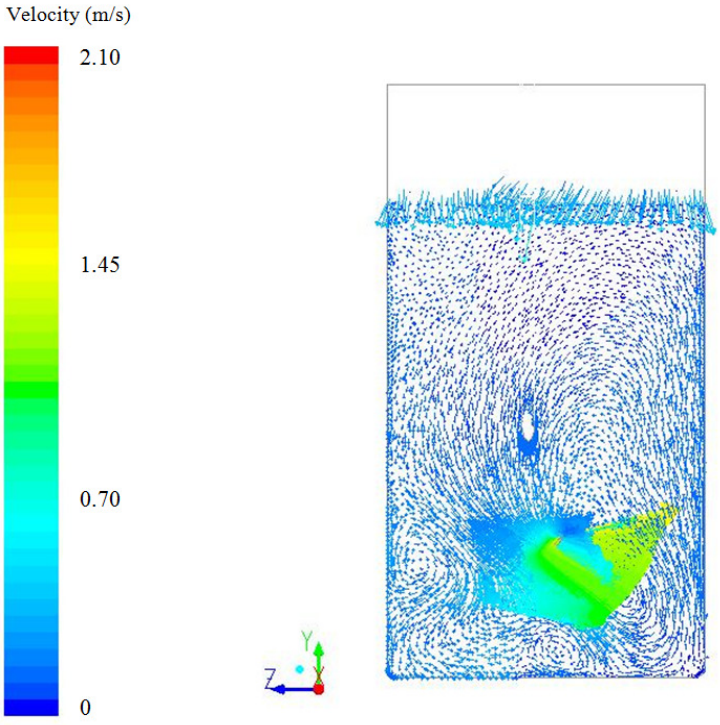

Fig. 12: Side plane velocity vectors for original Case A1.

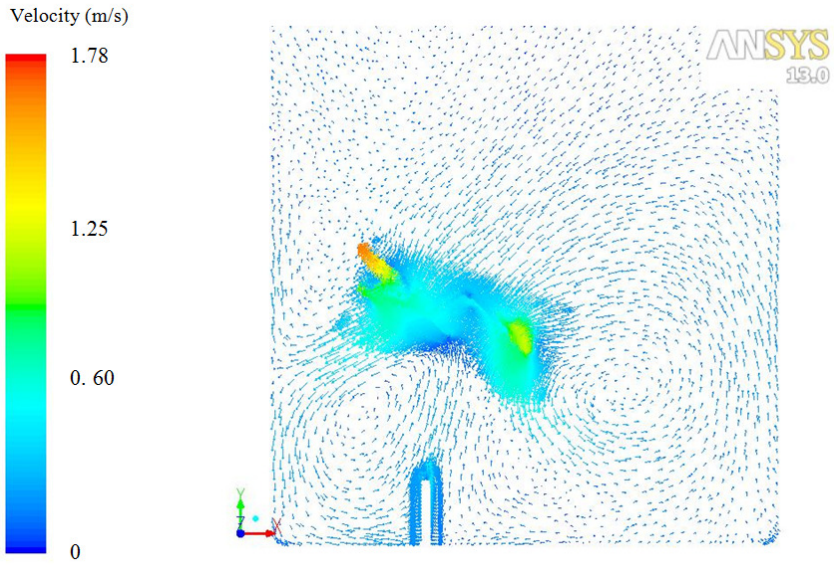

Fig. 13: Close-up view of velocity vectors for Case B2.

Figures 14-16 show several representative cases' particle pathlines, or the paths the oxygen bubbles would follow in the simulation. These show the path of particles released during the simulated process and the path they would follow the flow, as computed. The particles are released from the inlet frit where the bubbles are released into the surrounding liquid. The particles seem to swirl as they are initially carried into the impeller, then outward and upward as can be seen. Some of the particles seem to get trapped in the flow and return down towards the bottom of the container or back through the impeller.

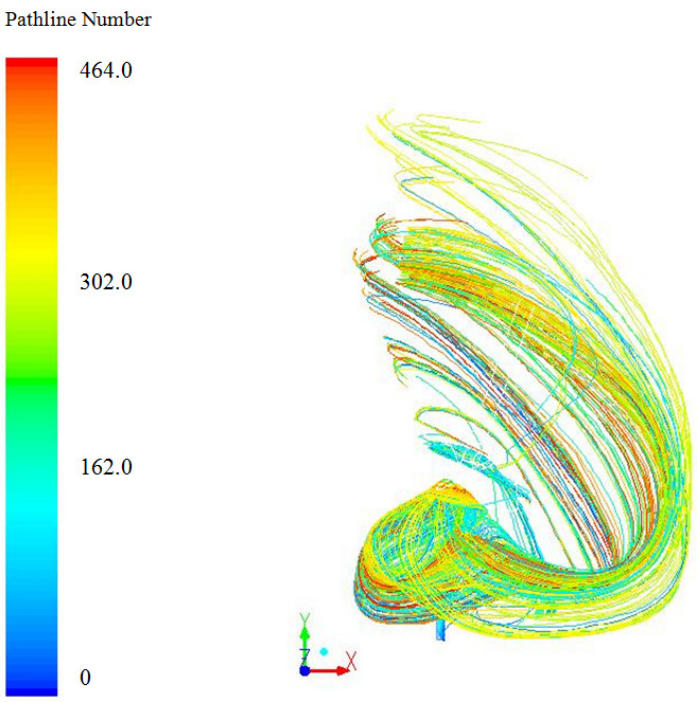

Fig. 14: Pathlines of bubbles in simulation for Case B2.

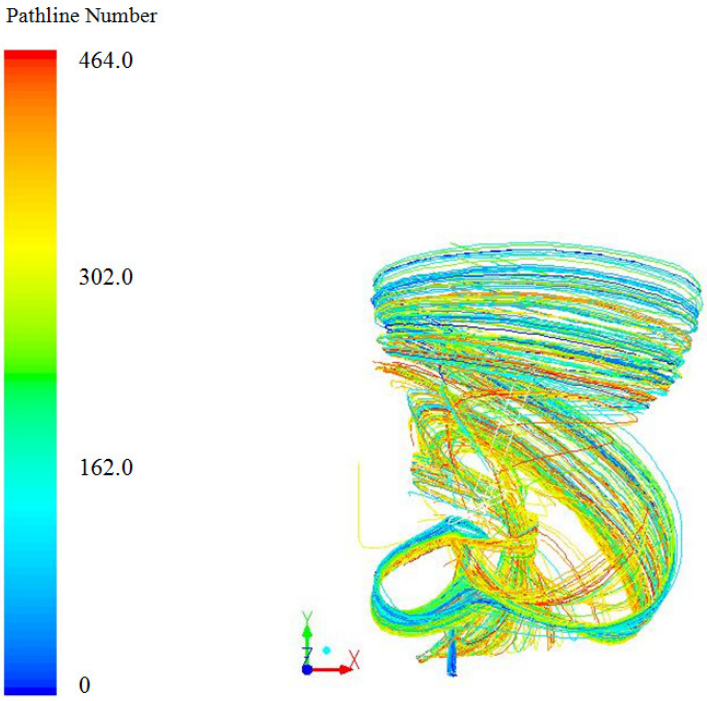

Fig. 15: Pathlines of bubbles in simulation for Case E1.

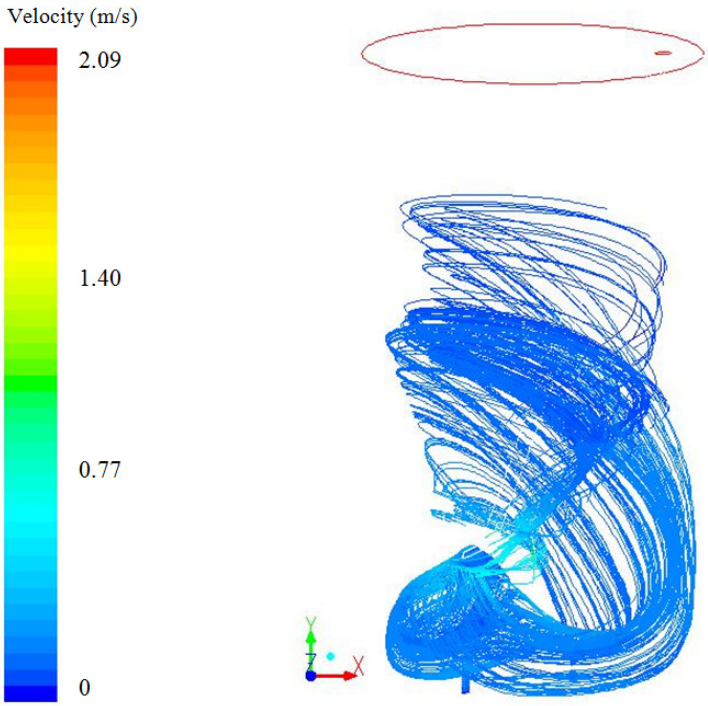

Fig. 16: Pathlines of bubbles in simulation for original Case A1.

Once the many different cases were configured as desired, the cases were run for several thousand iterations in order to achieve convergence. The exact number of iterations required to reach convergence differs from case to case. In total, more than 200,000 iterations were run in total, with each single case being run for 8,000 – 17,000+ iterations. In the end, most of the cases did converge, at least conditionally. There were a few cases which did not converge and they are noted as such.

Several important calculated numbers, including the mass transfer coefficient were recorded and output to a .txt file along with the iteration number for each case, as specified iteration intervals. This output was written every 10 iterations for tracking the convergence of the mass transfer coefficient. This allowed the tracking of the convergence of each case, making it easier to see when a case was diverging, so it could

be stopped and modified as needed. The cases were tracked until this mass transfer coefficient was converged to about two orders of magnitude. Some of the cases did converge to more than two orders of magnitude, but for this comparison, two orders of magnitude are deemed sufficiently accurate. This would be more accurate than could reasonably be expected for most experimental measurements of this type. Table 3 lists the different cases run, number of iterations run, and the calculated mass transfer coefficients.

The mass transfer coefficient $K_l a$ is calculated in the same way Kerdouss et al. [7] and Dhanasekharan et al. [9] calculated this variable. Thus, K_l can be calculated from the following equation:

$$K_l = \frac{2}{\sqrt{\pi}} \sqrt{D_{O_2}} \left(\frac{\varepsilon \rho_L}{\mu_L} \right)^{0.25} \tag{29}$$

where D_{O_2} represents the diffusion coefficient of oxygen for this case (since oxygen is the gas phase substance). As in Spall et al. [8] this was taken as 2.01 x 10^{-9} m^2/s. The variable ε is the turbulence dissipation rate, ρ_L is the density and μ_L is the dynamic viscosity of the liquid phase (water for this case).

The interfacial area is the surface area between the bubbles of oxygen and the surrounding water. This area is calculated from:

$$a = \frac{6\alpha_G}{d_{32}} \tag{30}$$

where α_G is the local gas volume fraction, given by:

$$\alpha_G = \frac{V_{O_2}}{V_{H2O}} \tag{31}$$

Here d_{32} is the sauter mean bubble diameter. This mean bubble diameter is calculated from:

$$d_{32} = \frac{\sum_i n_i d_i^3}{\sum_i n_i d_i^2} \tag{29}$$

where n_i is the number density and d_i is the diameter of the ith bubble class. As mentioned previously, the values for K_l and a are calculated separately for this work. The results from these calculations are then multiplied and the product is the volume-averaged $K_l a$ variable. This approach is different than calculating the $K_l a$ by volume averaging the K_l and a values separately [8].

Table 3: Cases run with corresponding numbers of iterations run and calculated $K_l a$ coefficients.

Case Name	Iterations Run	$K_l a$
A1	0	8.69
B1	8990	6.86
B2	9090	13.10
B3	9090	25.60
B4	9070	23.80
C1	8600	4.94
C2	8600	4.94
C3	*n/a*	*Not converged*
C4	9600	4.84
D1	8590	7.09
D2	8590	9.30
D3	*n/a*	*Not Converged*
E1	8580	13.55
E2	8910	8.76
E3	9090	18.46
E4	9090	5.40
F1	17200	7.15
F2	16590	4.77
F3	17200	7.28
F4	17200	7.19

The cases in Table 3 which did not converge were not pursued further, as sufficient data was available from the other cases for the purposes of this report. The results in Table 3 show that in most cases, a good estimate of the mass transfer coefficient *might* be achieved based on current bubble aggregation and breakup models. This however, can also be grossly incorrect depending only on the bubble aggregation and breakup models chosen. If the user had no prior experience or comparison data (experimental measurements) to compare to, it would be impossible to know if the results were at all reliable. It is also interesting to note that in general, larger numbers of bubble bins led to larger calculated mass transfer coefficient values.

The experimental data for $K_l a$ numbers provided by Stoker et al. [11] for comparison is given in Table 4. These measurements were taken with a setup having the same size 250-L tank and the same impeller rotation rate of 118 RPM. These cases are identical in operating conditions to those modeled using CFD methods. It is interesting to note that with the following results, there were 6 different repetitions made, with measurements being taken and values calculated for each of the 6 reps. There seems to be a good agreement in the calculated mass transfer coefficient for most of the cases, except for the 0.04 vvm (gas volume flow per liquid volume per minute) aeration rate, where there is more spread in the calculated $K_l a$ coefficient. The CFD cases run here were run with a gas flow rate of 2.5 lpm, which is equivalent to 0.01 vvm. For the CFD cases presented herein, the majority of the converged cases are within about +/- ~1 (t^{-1}) or more for the $K_l a$ coefficient. This difference is more than 20% for some cases, which is a very significant difference. There is a very definite correlation between the aeration rate and the measured $K_l a$ coefficient. Higher aeration rates lead to higher $K_l a$, which is expected.

Table 4: Experimentally measured $K_l a$ coefficients.

Aeration Rate (vvm)	0.02	0.03	0.04
Rep 1	5.832	7.308	11.34
Rep 2	5.94	7.02	11.052
Rep 3	6.228	7.272	10.764
Rep 4	6.336	7.812	9.18
Rep 5	6.516	7.884	9.216
Rep 6	6.372	7.956	9.216

The results of the present CFD cases do agree in general magnitude with the measured and computed quantities presented by Stoker et al., but not sufficiently reliable for use at the present time. Depending on the choice of bubble coalescence and bubble breakup models, there exists a possibility of either being close to the correct value (as compared to the measured value), or being quite far from it. Results with such a large spread would be completely unreliable for prediction purposes.

The cases which seem to have predicted the closest $K_l a$ values are Cases B1, D1, F1, F3, and F4. Cases F1, F3, and F4 with the Turbulent aggregation model and the Luo, Ghadiri, and Laakkonen models, respectively, have predicted close values of 7.15, 7.28, and 7.19, respectively. Another close prediction is given by Case B1 with 7 bubble bins, the Luo aggregation model, and the Lehr breakup model. Case B1 predicted a $K_l a$ value of 6.86. Cases D1 with the Luo aggregation and Luo breakup models also predicted a $K_l a$ value of 7.09. Out of the 20 cases run, only 5 of them have predicted these somewhat-close values.

The cases which were run with constant diameter bubbles had very little difference in the computed $K_l a$ coefficient. There does seem to be a slight dependence of $K_l a$ on the

bubble diameter, which should be the case. In Case C4, the computed $K_l a$ value is slightly lower for cases with larger bubble diameter. This is likely due to the decrease in interfacial bubble area with larger bubble diameters. Perhaps with larger differences in bubble diameter for the constant diameter cases, there would be a more noticeable difference in the computed $K_l a$ coefficient.

The several different cases involving different combinations of bubble breakage and aggregation kernel functions predicted very different mass transfer coefficients, simply depending on what combination of models is chosen. The difference in the lowest and the highest $K_l a$ computed is approximately 20, which is more than 5 times larger than the smallest $K_l a$ number calculated. The average of all these $K_l a$ from Table 3 is calculated to be 9.14, with the standard deviation being 5.62. This spread of $K_l a$ is insufficient for anyone to rely on without experimental measurements to validate the numbers. Based on the experimental numbers from Stoker et al., the average of the values they measured and calculated for $K_l a$ was 7.96, for the same setup and operating conditions as this CFD model incorporates. These experimental measurements include a standard deviation of 1.78.

CHAPTER X

CONCLUSIONS

While all the cases run did not converge, most of them did. It is possible from these results to draw sufficient conclusions about the ability of the current mathematical models. These models for bubble breakage and aggregation kernel functions do not seem to be sufficient in computing the mass transfer coefficient for this type of two-phase process. The spread of results encountered is too wide to rely on the results with any degree of certainty.

The cases which were run with single diameter, constant diameter bubbles came out as expected, with larger bubble diameters having lower mass transfer coefficients (due to the lower overall interfacial bubble area). The results show that there is a clear dependency of the $K_l a$ number on the bubble size, and therefore the bubble interfacial area, which clearly should be the case.

It would be conceivable for this type of simulation to be validated with experimental measurements, however, that process can be expensive and time-consuming for any reliable results. It would take a significant amount of time to adjust the necessary parameters and run the necessary iterations to ensure convergence of the results, along with the necessary computer resources. At the present time, numerical models for bubble aggregation and coalescence are not sufficient to accurately predict $K_l a$ numbers.

REFERENCES

[1] Gigas, B., and Dhanasekharan, K., "Breathing Life into Bioreactors," *FLUENT NEWS*, Fall 2003 Edition, URL: http://www.fluent.com/about/news/newsletters/03v12i2_fall/s5.htm [cited 11 November 2011].

[2] Fang, Z., "Applying Computational Fluid Dynamics Technology in Bioprocesses - Part 1," Biopharminternational.com, April 1, 2010, Vol. 23, Issue 4, URL: http://biopharminternational.findpharma.com/biopharm/article/articleDetail.jsp?id=663865&pageID=1&sk=&date= [cited 11 November 2011].

[3] Bayraktar, E., Mierka, O., Platte, F., Kuzmin, D., and Turek, S., "Modeling and Numerical Aspects of Population Balance Equations in Gas/Liquid-Liquid Two Phase Flows," *Institute of Applied Mathematics (LS III)*, Dortmund, Germany.

[4] Lehr, F., Millies, M., and Mewes, D., "Bubble-Size Distributions and Flow Fields in Bubble Columns," *Fluid Mechanics and Transport Phenomena*, Institute of Process Engineering, Hannover, Germany, Vol. 48, No. 11, November 2002, pp. 2426-2443.

[5] Lehr, F., and Mewes, D., "A Transport Equation for the Interfacial Area Density Applied to Bubble Columns," *Chemical Engineering Science,* Vol. 56, 2001, pp. 1159-1166.

[6] Millies, M., and Mewes, D., "Interfacial Area Density in Bubbly Flow," *Chemical Engineering and Processing,* Vol. 38, 1999, pp. 307-319.

[7] Kerdouss, F., Bannari, A., Proulx, P., Bannari, R., Skrga, M., and Labrecque, Y., "Two-phase Mass Transfer Coefficient Prediction in Stirred Vessel with a CFD

Model," *Science Direct, Computers and Chemical Engineering,* Vol. 32, 2008, pp. 1943-1955.

[8] Spall, R., Jones, N., and Staheli, C., "Computational Fluid Dynamics Analysis of Fluid Mixing in Single Use Bioreactors," *ASME International Mechanical Engineering Congress and Exposition*, November 12-18, 2010, Vancouver, British Columbia

[9] Dhanasekharan, K.M., Sanyal, J., Jain, A., and Haidare, A., "A generalized approach to model oxygen transfer in bioreactors using population balances and computational fluid dynamics," Chemical Engineering Science, Vol. 60, 2005, pp. 213-218.

[10] ANSYS, Inc., "ANSYS FLUENT Population Balance Module Manual, " ANSYS Release 13.0, Canonsburg, PA, Copyright 2010.

[11] Private Communications, Emily Stoker et al., 2011.